

Supporting Information

Enhanced Cathode Integrity for Zinc-Manganese Oxide Fiber Batteries by a Durable Protective Layer

1. Finite Element Analysis

The finite element analysis was used to simulate the stress distribution in MnO₂ layer of pristine MnO₂ cathodes and MnO₂ with CNT film during bending deformation, using the commercial software ABAQUS.¹ In the simulation, the bulk modulus and Poisson's ratio of MnO₂ were 34.4 GPa and 0.3, and the elastic modulus and Poisson's ratio of CNT film were 10 GPa and 0.3, respectively. The current collector part was a cylinder with a radius of 0.5 mm and a length of 20 mm. The simulated MnO₂ part was a hollow cylinder with an inner diameter of 0.5 mm, an outer diameter of 0.51 mm and a length of 20 mm. The CNT film had the same length, but with the inner diameter of 0.51 mm and an outer diameter of 0.52 mm. Three support models were built to make the fiber curve (Figure S14a). In order to make the model curve, the cylinder in the middle was set to move vertically down 5 mm, while the two bottom supports were constrained in all degrees of freedom. Two ends of model were fixed in z-direction but were free in x-y plane (Figure S14b). In the analysis process, the MnO₂ was meshed with 3D stress elements (C3D8R) and the CNT film was meshed with shell elements (S4R), respectively. A mesh convergence analysis was performed and a mesh size of 0.2 mm was chosen to balance the accuracy and computational cost. The stress distribution results conformed to von Mises yield criterion.

2. CV Study

Figure S23 displayed the CV curves of the Zn-CMCP batteries at different scan rates (0.1, 0.2, 0.5, 0.8 and 1.0 mV s⁻¹) with a voltage range from 0.8 to 1.8 V. The peak current and scan rate had the following relationship:

$$i = av^b,$$

which could also be re-written as:

$$\log(i) = b\log(v) + \log(a),$$

where b could be viewed as the slope of a line with $\log(v)$ as its independent variable and $\log(i)$ as its dependent variable. b value was related to the state of the electrode reaction in the battery. When b was 0.5, the current came from the Zn^{2+} diffusion. When b was 1, the battery capacity came from the capacitance effect. After fitting the four charge/discharge peaks, the b values obtained were 0.865, 0.749, 0.718, and 0.888 for Peak 1, 2, 3 and 4, respectively, indicating that the ionic diffusion and pseudocapacitance both existed in the electrochemical process of Zn/CMCP batteries, indicating the battery showed good rate performance. Figure S24a showed that the electrochemical performance of Zn-CMCP battery was deconvoluted into contributions of ionic diffusion and surface capacitive in a quantitative manner. The capacitive contribution gradually increased to 93.7% upon the increasing scan rate from 0.1 to 1.0 mV s^{-1} (Figure S24b), validating the improved kinetics and high surface reactivity.²

3. ICP Analysis

ICP (Inductive Coupled Plasma Emission Spectrometer) was used to detect the concentration of Mn^{2+} in the electrolyte during bending or charging and discharging to calculate the amount of MnO_2 dissolved into the electrolyte, that was, the amount of the active material detached from the current collector. The electrolyte for ICP tests only contained 2 M ZnSO_4 to exclude the interference of the original manganese ions on the test results.

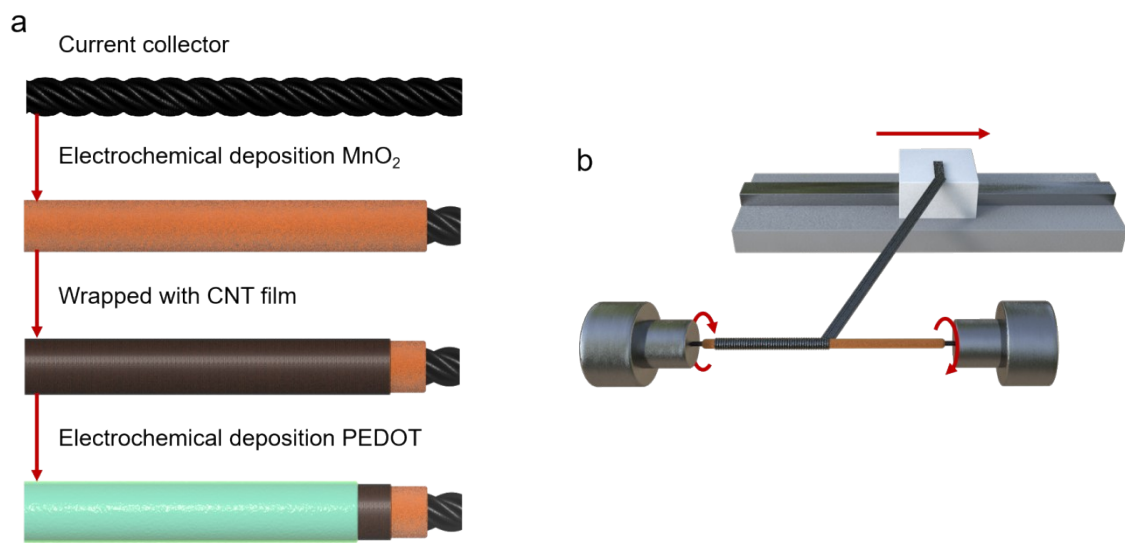


Figure S1. a, b) Fabrication process of the CMCP cathode and the CNT film wrapping process on the CM fiber.

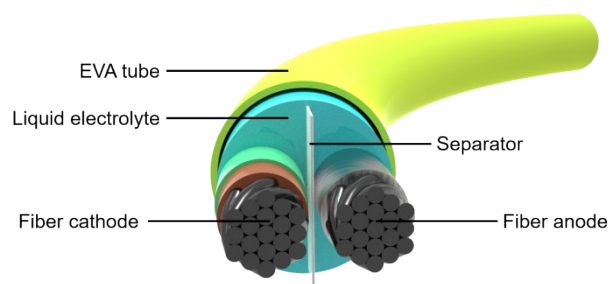


Figure S2. Schematic diagram of the Zn-CMCP fiber battery. A separator strip was inserted between the cathode and anode fibers to prevent the short circuit of the full fiber battery.

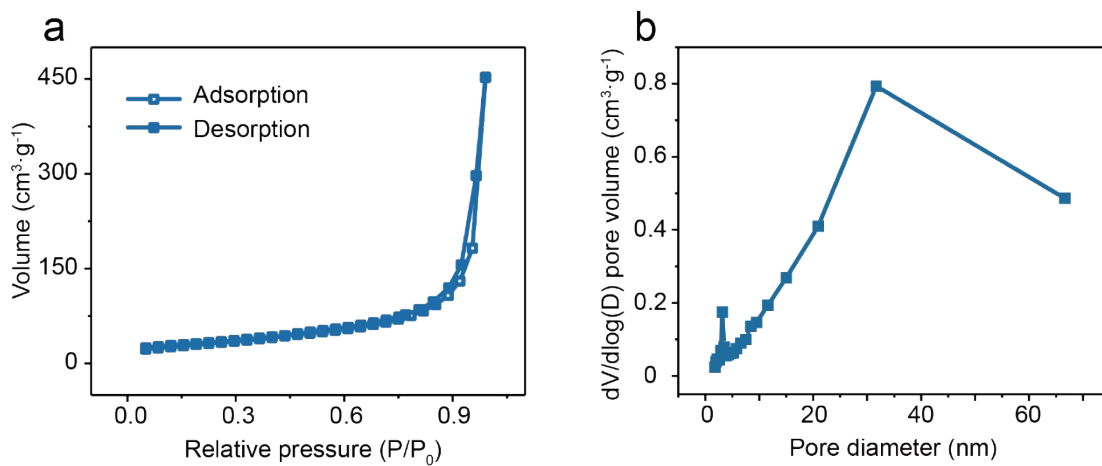


Figure S3. a, b) N₂ adsorption/desorption isotherm (measured at 77 K) and pore size distribution of the current collector fiber. The specific surface area of the was 113.6 m² g⁻¹.

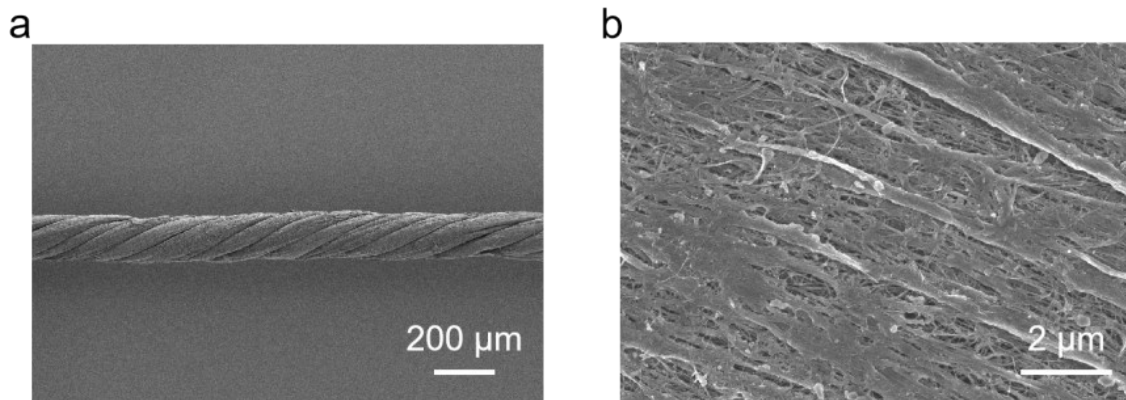


Figure S4. a, b) SEM images of multi-ply CNT fibers in low and high magnifications.

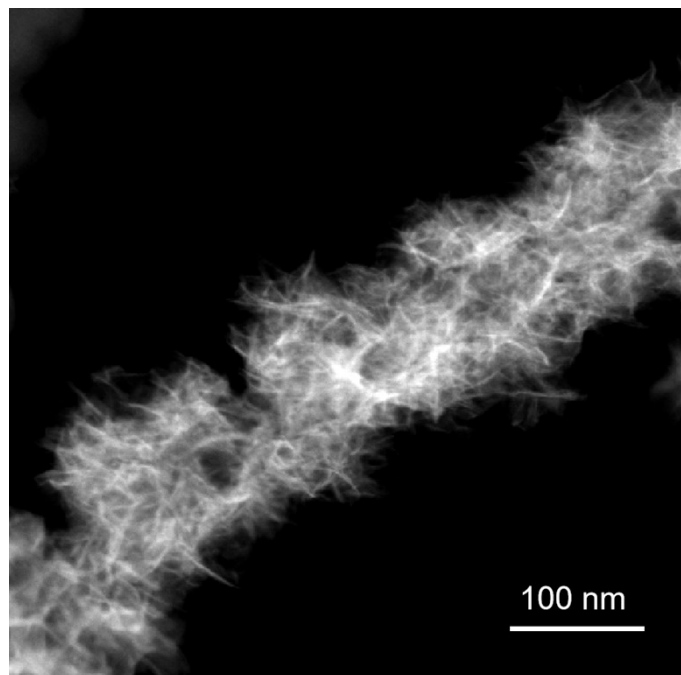


Figure S5. The dark-field TEM image of CM.

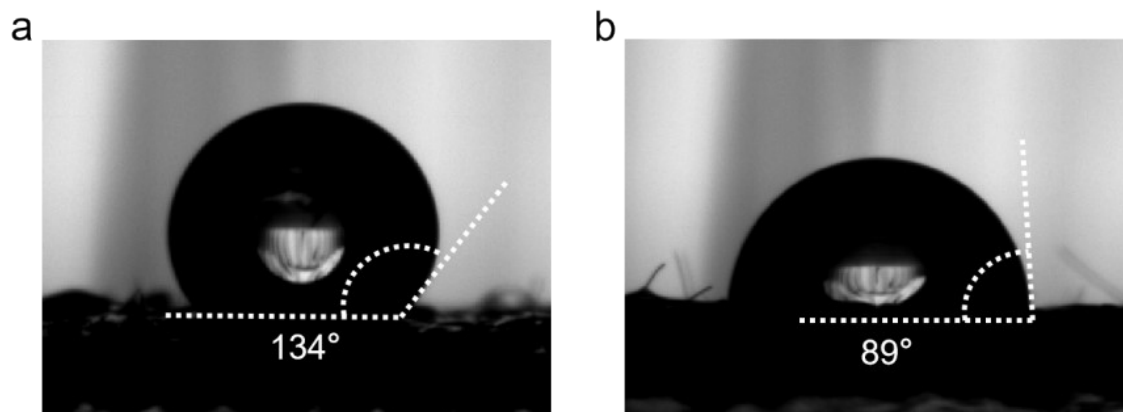


Figure S6. a, b) Contact angle tests of CMC and CMCP.

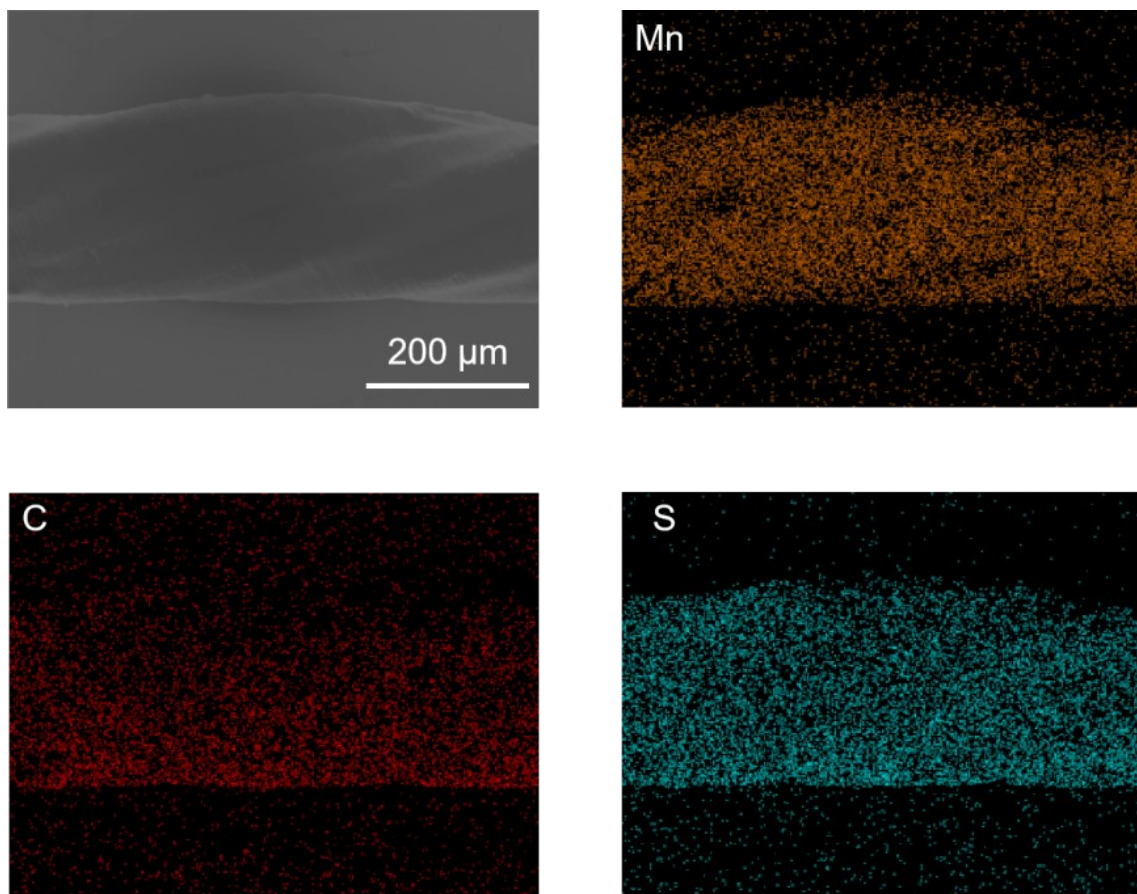


Figure S7. SEM elemental mappings of Mn, C, S of the CMCP.

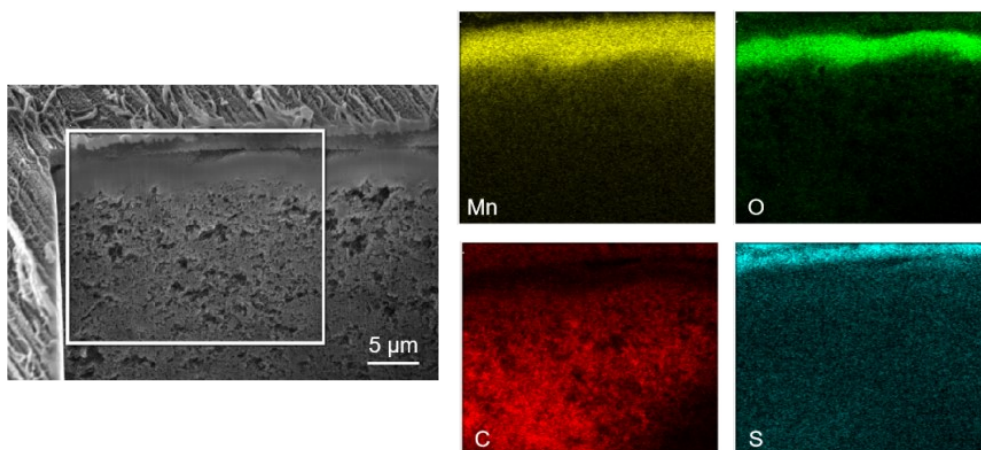


Figure S8. SEM elemental mappings of the cross section of CMCP.

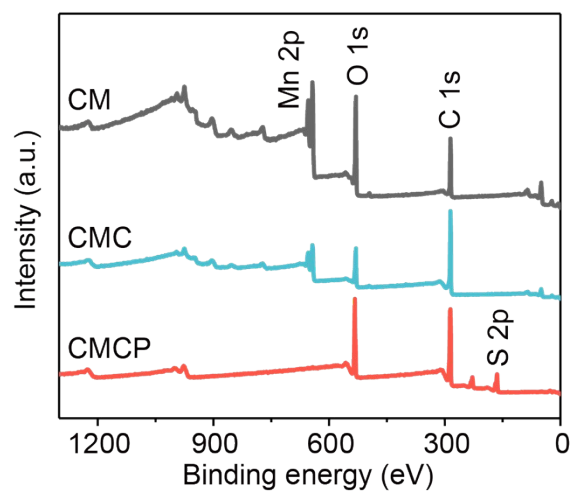


Figure S9. XPS survey spectra of CM, CMC, and CMCP.

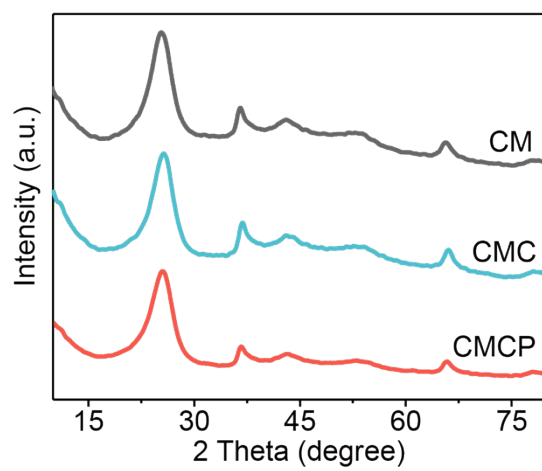


Figure S10. XRD patterns of CM, CMC, and CMCP.

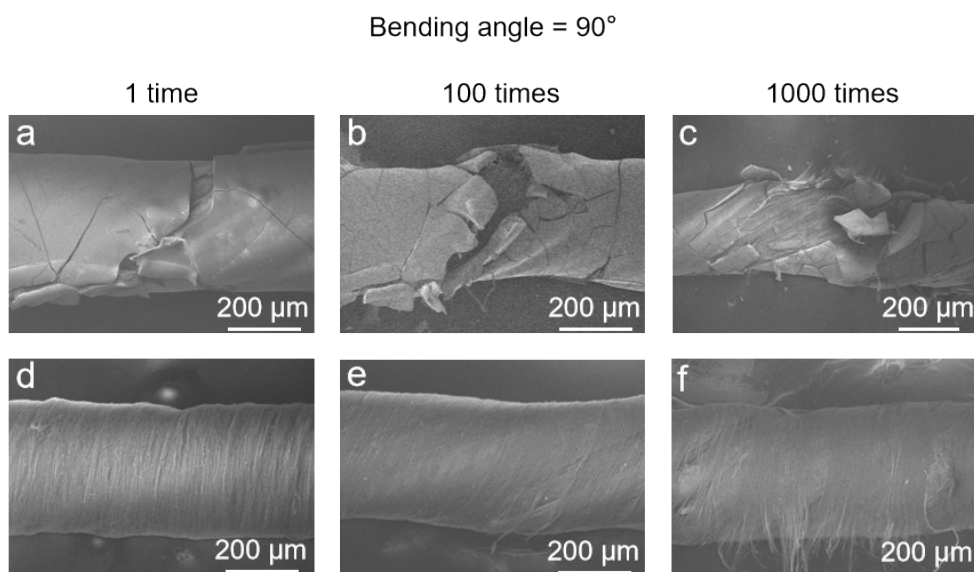


Figure S11. a-c) SEM images of CM fiber cathode under 90° bending angel after 1, 100, 1000 bending times. d-f) SEM images of CMC fiber cathode under 90° bending angel after bending 1, 100 and 1000 times.

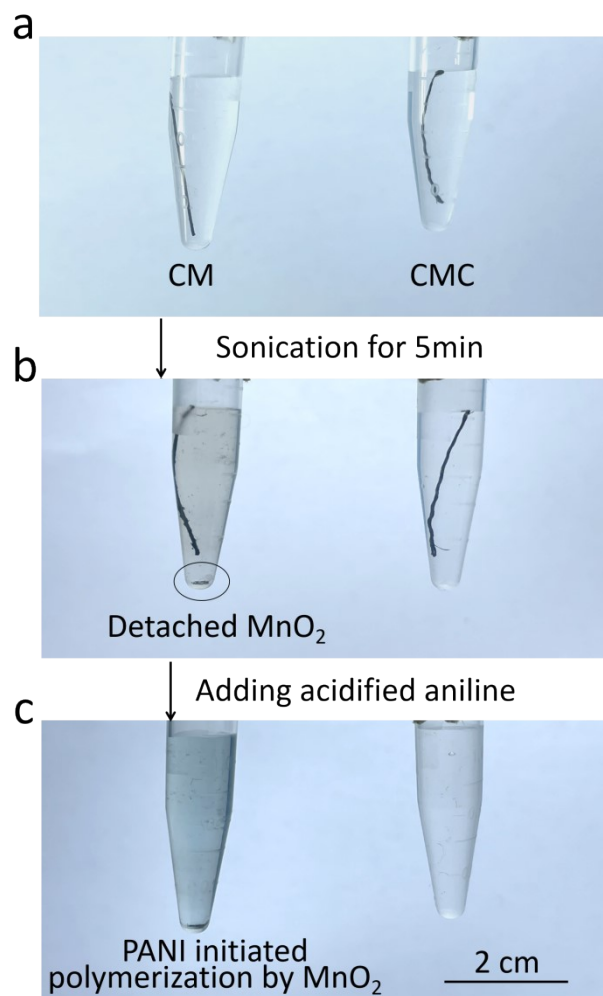


Figure S12. a) CM and CMC in deionized water, b) CM and CMC after 5 min ultrasonic treatment in deionized water, and c) ultrasonic solutions after adding acidified aniline.

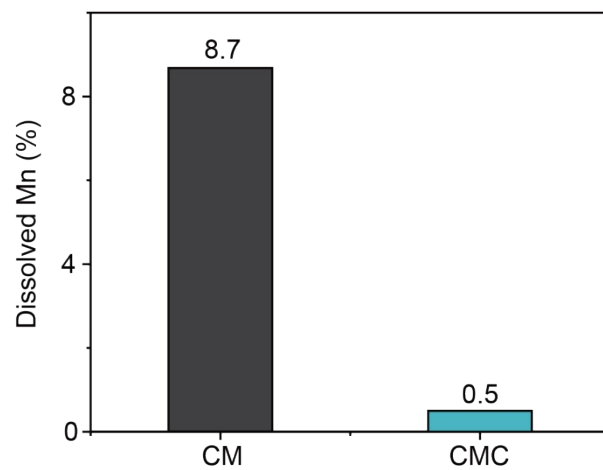


Figure S13. Element analysis of Mn in deionized water of CM and CMC after ultrasonic vibration experiment.

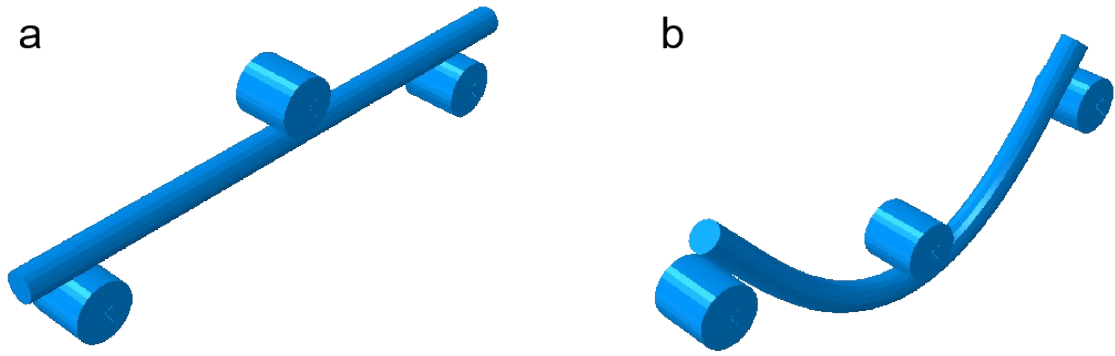


Figure S14. a, b) The model of fiber before and after bending.

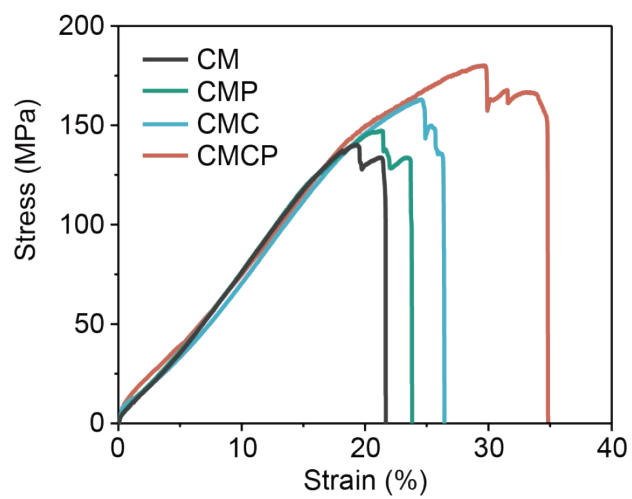


Figure S15. Stress-strain curves of different fiber cathodes.

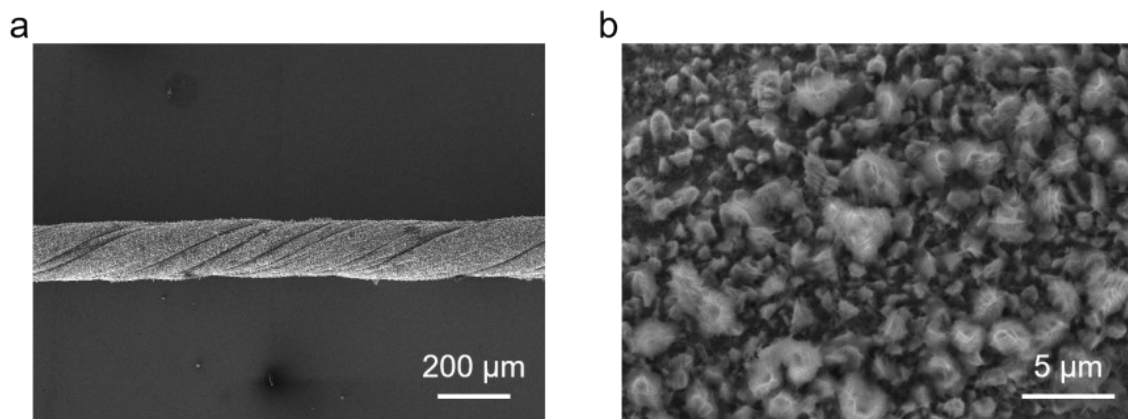


Figure S16. a, b) SEM images of Zn anode at low and high magnifications.

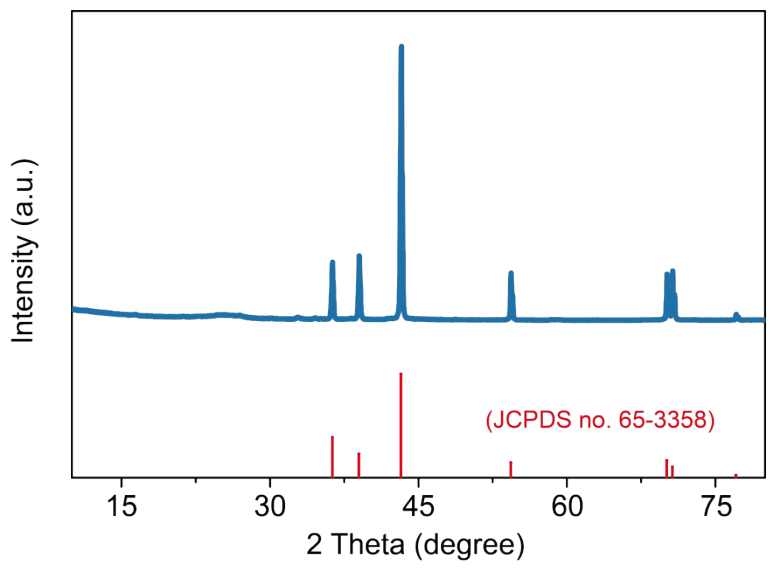


Figure S17. XRD pattern of Zn anode.

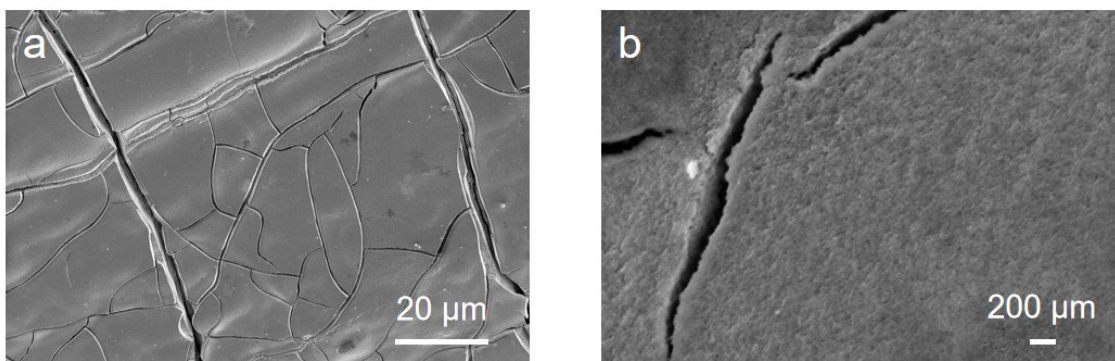


Figure S18. a, b) SEM images of CMP fiber cathode at low and high magnifications.

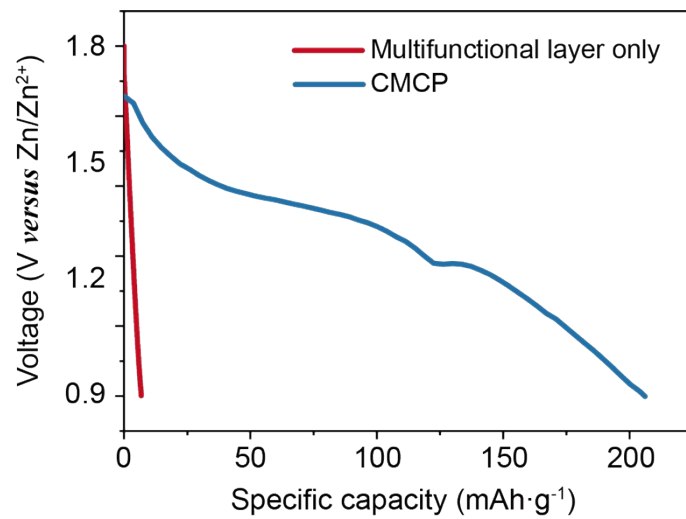


Figure S19. Charge/discharge curves with and without MnO₂ at 1 A g⁻¹.

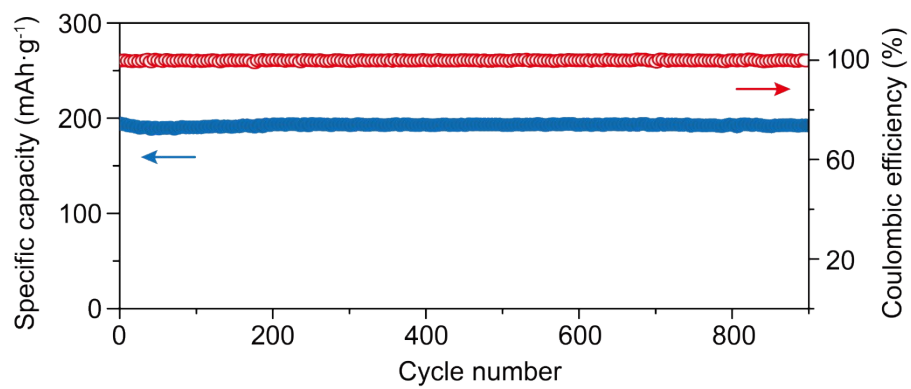


Figure S20. Cycling performance of CMCP at 1 A g⁻¹ and corresponding CE.

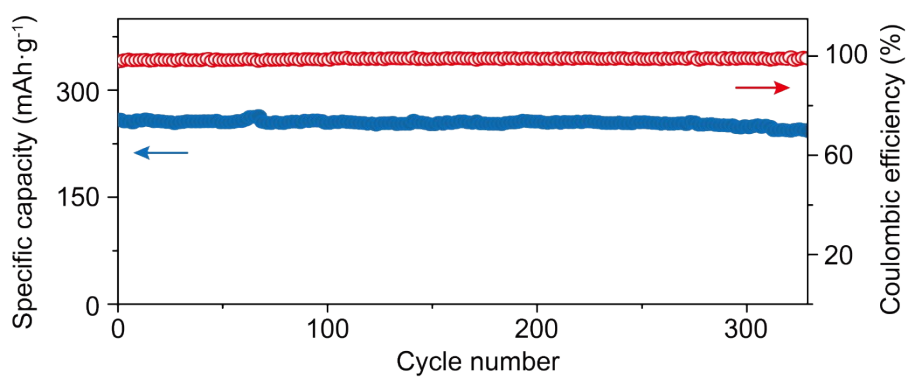


Figure S21. Cycling performance of CMCP at 0.5 A g⁻¹ and corresponding CE.

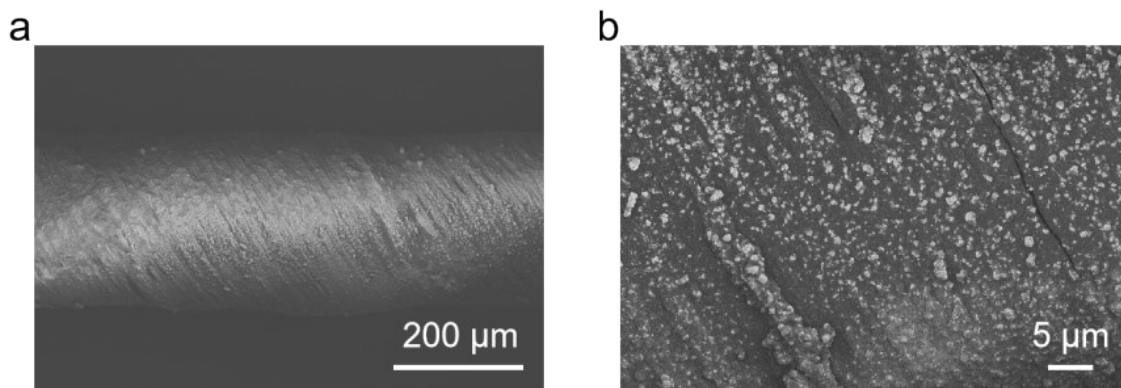


Figure S22. a, b) Surface morphology of cycled CMCP electrode in low and high magnifications.

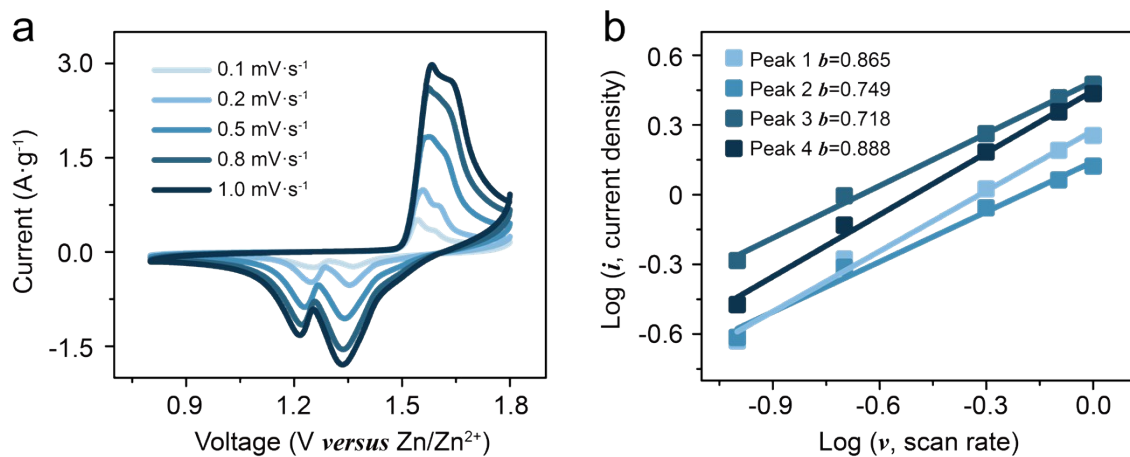


Figure S23. a) CV curves of CMCP at increasing scan rates from 0.1 to 1.0 mV s^{-1} and b) plots of $\log(i)$ versus $\log(v)$ of the cathodic current response at four peaks of CMCP labeled in (a).

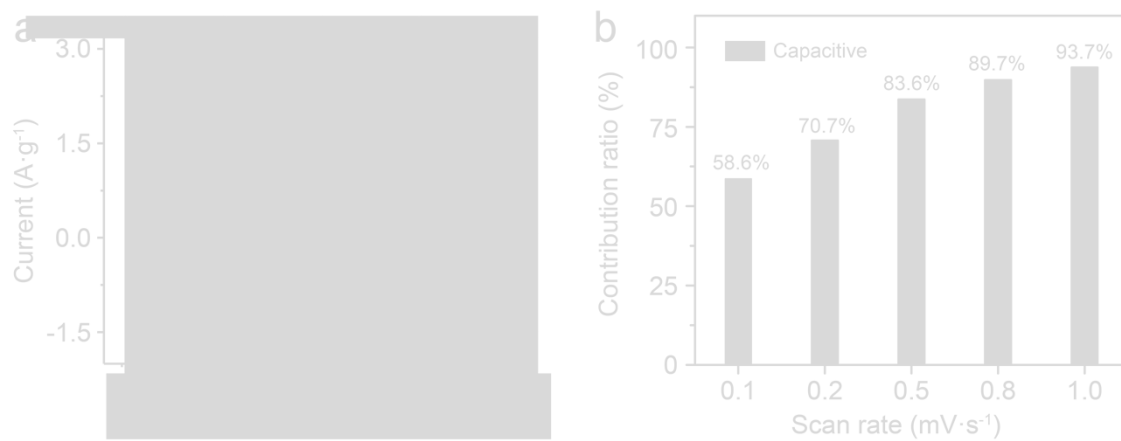


Figure S24. a) Capacitive contribution to the total capacity at 1 mV s⁻¹ of CMCP and b) capacity contribution ratio of CMCP at different scan rates.

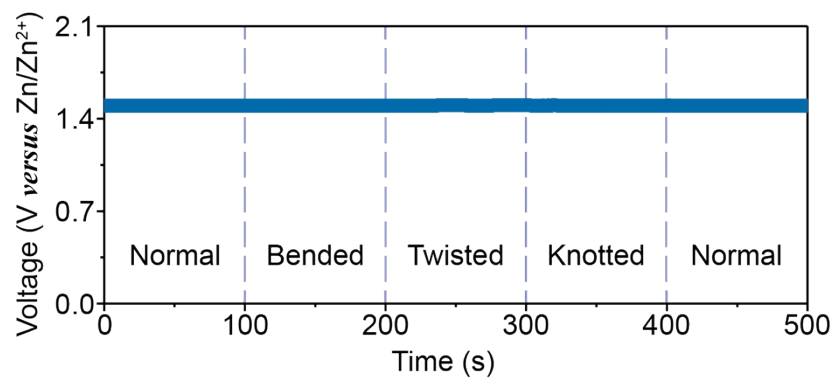


Figure S25. Open circuit voltage of the CMCP under different deformations.

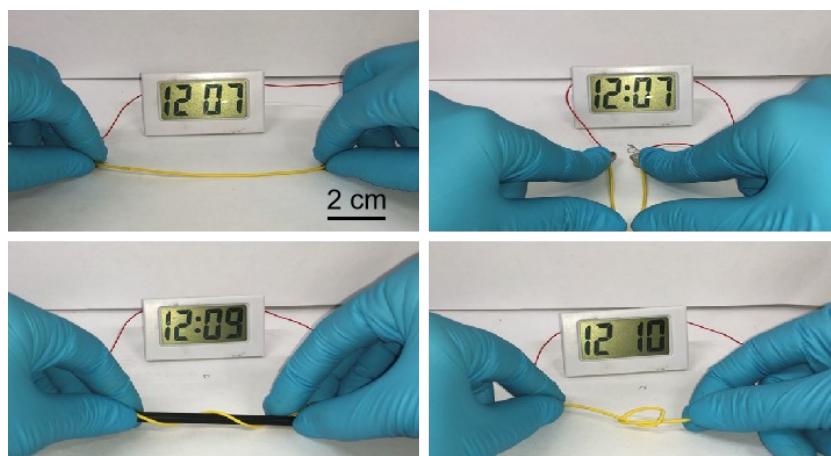


Figure S26. Photographs of a fiber CMCP under various deformations.

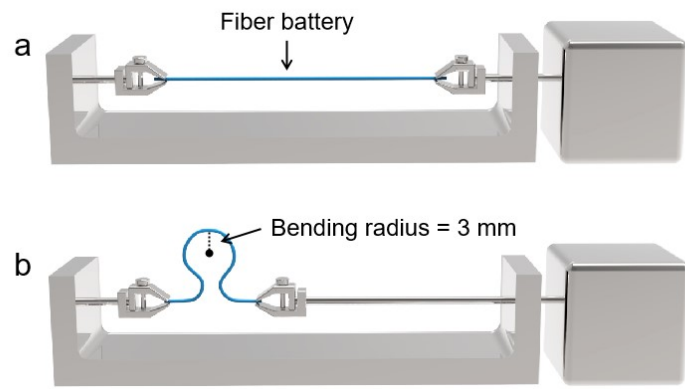


Figure S27. Schematic of the home-made step motors for bending test in Figure 4c. The fiber batteries were bended with a bending radius of 3 mm and under different bending angles.

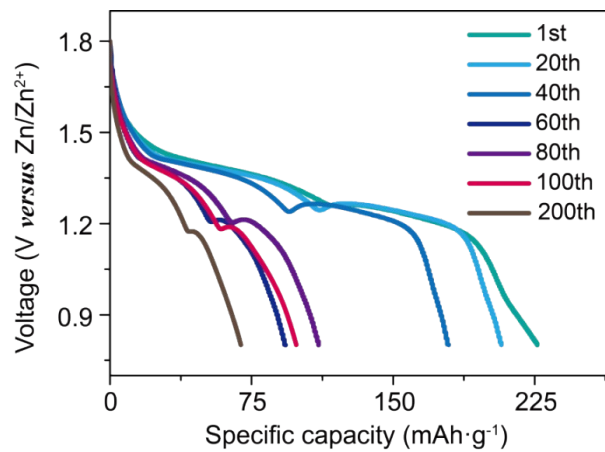


Figure S28. Galvanostatic discharge curves of CM after different bending cycles at 1 A g⁻¹.

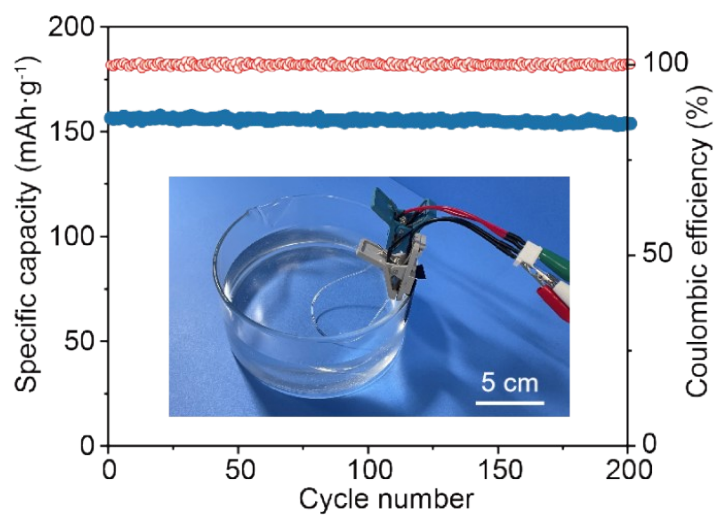


Figure S29. The excellent water-proof performance of fiber battery because using the water-proof packaging material.

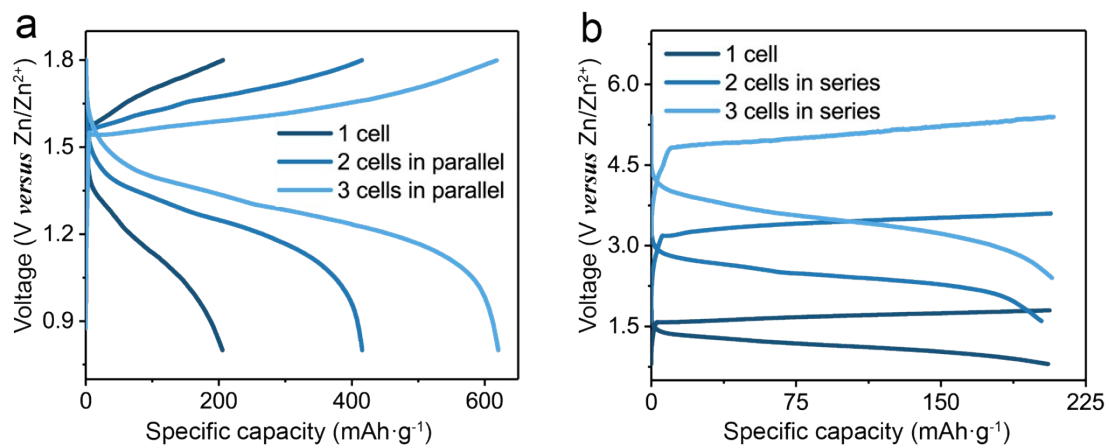


Figure S30. a, b) Charge/discharge curves of CMCP connected in parallel and in series measured at 1 A g⁻¹.

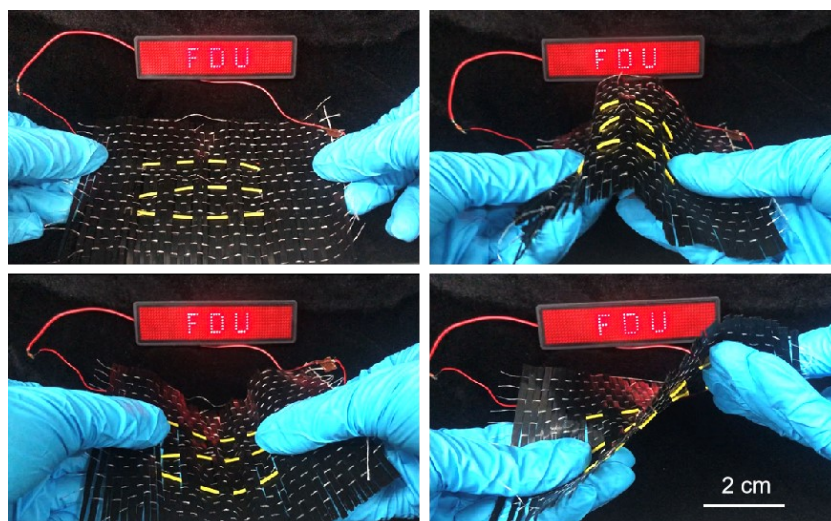


Figure S31. Photographs of three fiber CMCPs connected in series powering a light-emitting diode display screen under various deformations.

References

1. L. Xu, X. Fu, F. Liu, X. Shi, X. Zhou, M. Liao, C. Chen, F. Xu, B. Wang, B. Zhang and H. Peng, *J. Mater. Chem. A*, 2020, **8**, 5476-5483.
2. J. Wang, J. Polleux, J. Lim and B. Dunn, *J. Phys. Chem. C*, 2007, **111**, 14925-14931.